ACS APPLIED MATERIALS & INTERFACES

www.acsami.org

Research Article

Nano-optomechanical Resonators for Sensitive Pressure Sensing

Yanping Chen, Shen Liu,* Guiqing Hong, Mengqiang Zou, Bonan Liu, Junxian Luo, and Yiping Wang

Cite This: *ACS Appl. Mater. Interfaces* 2022, 14, 39211−39219

Read Online

ABSTRACT: Nanomechanical sensors made from suspended graphene are sensitive to pressure changes. However, these devices typically function by obtaining an electrical signal based on the static displacement of a suspended graphene membrane and so, in practice, have limited sensitivity and operational range. The present work demonstrates an optomechanical Au/graphene membrane-based gas pressure sensor with ultrahigh sensitivity. This sensor comprises a suspended Au/graphene membrane appended to a section of hollow-core fiber to form a sealed Fabry−Pérot cavity. In contrast to conventional nanomechanical pressure sensors, pressure changes are monitored via resonant sensing with an optical readout. A miniature pressure sensor based on this principle was able to detect an ultrasmall pressure difference of 1×10^{-7} mbar in the ultrahigh-vacuum region with a pressure range of 4.1×10^{-5} to 8.3×10^{-6} mbar. Furthermore, this pressure sensor can work over an extended pressure range of 7×10^{-6} mbar to 1000 mbar at room temperature, outperforming commercial pressure sensors. Similar results were obtained using both the fundamental and higher-order resonant frequencies but with the latter providing improved sensitivity. This sensor has a wide range of potential applications, including indoor navigation, altitude monitoring, and motion detection.

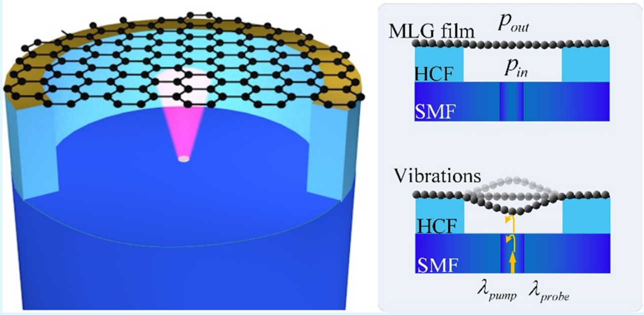

KEYWORDS: *nano-optomechanical, graphene, pressure sensor, gas damping, fiber optic sensors*

1. INTRODUCTION

Nanomechanical resonators have attracted considerable interest in recent years. These devices have been widely used to measure force,[1] charge,[2,3] mass,[4−7] pressure,[8,9] magnetic and electronic phase transitions,[10] and thermal radiation[11] while demonstrating exceptional sensitivity. There is special interest in nanomechanical resonators based on suspended graphene because graphene has exceptional mechanical properties,[12] including extremely high mechanical strength, stiffness, and thermal conductivity along the basal plane. Graphene also exhibits excellent hermetic[9,13,14] and electrical[15] properties. For these reasons, graphene is an ideal candidate for pressure-sensing applications and various types of gas pressure sensors based on graphene have been proposed.

In the majority of conventional pressure sensors, the deflection of a membrane is used as an effective means of measuring pressure because the movement of the membrane is related to the pressure difference between the interior and exterior of a hermetically sealed reference cavity. Electrical readout systems based on electrical transconductance,[16,17] piezoresistivity,[18−20] or conductance[21,22] all provide highly sensitive sensing of the membrane motion. However, these electrical processes have associated challenges that are primarily related to parasitic capacitance and thermal−mechanical displacement noise. In comparison, optical readout systems provide the advantages of high resolution and fast response while mitigating the aforementioned limitations. Fiber-optic pressure sensors with optical readout systems, such as those devices based on Fabry−Pérot interferometers (FPI),[23−27] photonic crystal fibers (PCFs),[28] and fiber Bragg gratings (FBGs),[29,30] have attracted great interest and have been widely studied. Among them, the devices based on FPI are the most promising pressure sensors because of their flexible design and robust structure. Thus, researchers have made efforts to improve both the pressure sensitivity and range of FPI-based pressure sensors. For instance, Guo et al.[25] proposed to fabricate an diaphragm-based FPI at the fiber tip for pressure sensing, achieving a static pressure sensitivity of 12.4 nm/kPa. Wang et al.[24] reported an all-silicon dual-cavity fiber-optic pressure sensor, achieving a pressure sensitivity of ∼33.034 nm/kPa within an air pressure range of 20−280 kPa. Dong et al.[31] presented an FPI pressure sensor with an integrated fiber Bragg grating, exhibiting a pressure sensitivity of 501.4 nm/kPa. However, all of these studies have employed

Received: June 2, 2022
Accepted: August 2, 2022
Published: August 22, 2022

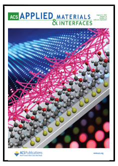

https://doi.org/10.1021/acsami.2c09865

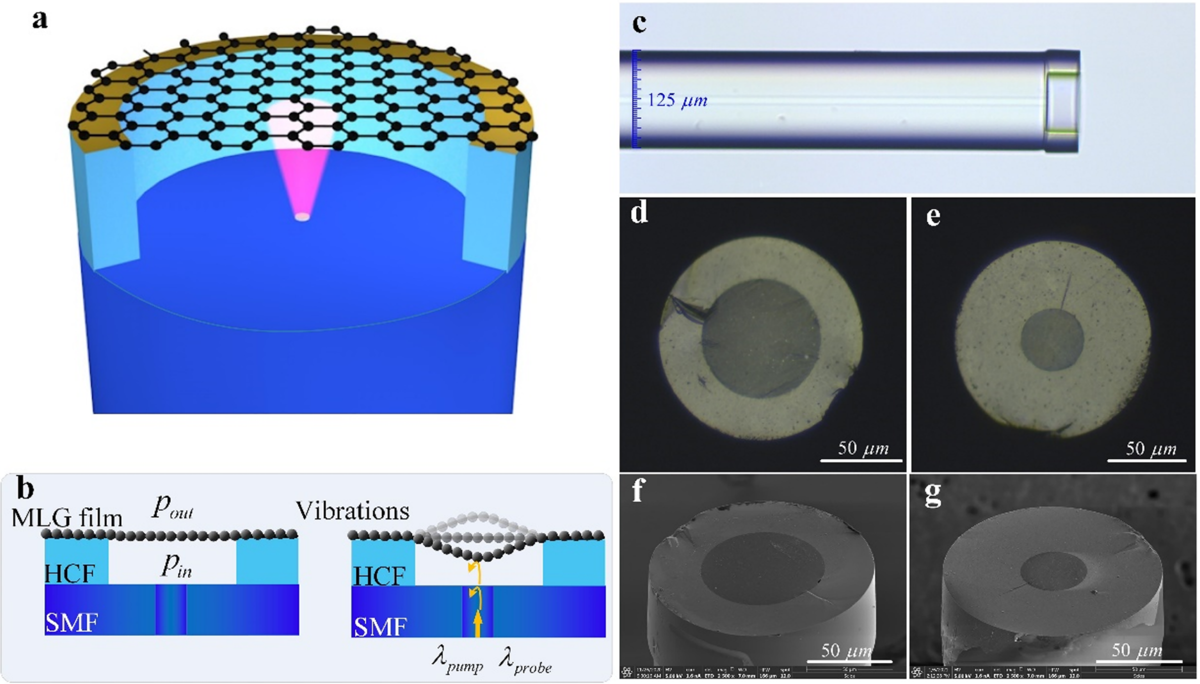

Figure 1. (a) Schematic of the optomechanical pressure sensor. (b) Detection of pressure-induced tension increases by monitoring the resonant frequency of the optomechanical resonator. (c) Side view of the sensor structure comprising an HCF segment attached to an SMF end. Top view optical microscopy images of sensor structures having inner diameters of (d) 75 and (e) 40 μm. Scanning electron microscopy images of the fiber tip resonators having inner diameters of (f) 75 and (g) 40 μm.

an optical-spectrum analyzer (OSA) as a measurement scheme, resulting in a limited pressure resolution.

In this work, we propose and demonstrate an optical fiber optomechanical resonator incorporating a multilayer graphene (MLG) membrane and Au membrane that is suitable for pressure sensing. In this device, both excitation and detection are based on all-optical systems. Changes in pressure modify the tension of the membrane and thereby shift its mechanical resonant frequency. Using the resonant frequency as the readout for pressure, we achieved an ultralow detectable pressure difference of 1×10^{-7} mbar in the ultrahigh-vacuum region with a pressure range of 4.1×10^{-5} to 8.3×10^{-6} mbar at room temperature. Furthermore, this pressure sensor can work over an extended pressure range of 7×10^{-6} to 1000 mbar. The calculated detectable pressure difference of the same device is $\sim 3.9 \times 10^{-8}$ mbar. This result was by far superior to that reported by the cavity length changes for the same Fabry-Pérot sensor.[31,32] We assessed two devices with inner diameters of 40 and 75 μm as pressure sensors. Because the results obtained with both diameters were similar, data for the device with an inner diameter of 40 μm are presented herein.

2. PRINCIPLE AND SENSOR FABRICATION

A diagram of the clamped circular Au/graphene membrane-based pressure sensor is shown in Figure 1a. The Au/graphene membrane and the fiber end facet both act as partially reflective mirrors and are separated by a section of hollow-core fiber (HCF) such that they form a low-finesse Fabry−Pérot cavity. The Au/graphene membrane mirror is moveable, while the fiber end facet mirror is fixed and the Fabry−Pérot cavity is sealed. Therefore, the pressure difference between the outside and the inside of the cavity greatly affects the tension of the membrane. Changes in tension, in turn, modify the resonant frequency, as shown in Figure 1b. The internal pressure of the unit can be greater than, equal to, or less than the external pressure. In the case that the external and internal pressures differ, the membrane will stretch as it deflects upward or downward as a result of this pressure difference, increasing the membrane tension. The tension will be at a minimum when the pressures outside and inside the cavity are equal. When the membrane stretches, the pressure difference ΔP applied on the Au/graphene membrane is balanced by the induced biaxial radial stress σ through the equation[33]

$$\Delta P \pi R^2 = \sigma 2\pi R t \tag{1}$$

where t and r are the thickness and the radius of the membrane, respectively. R is the curvature radius of the deflected membrane. The circular membrane deflects when subjected to a uniformly distributed pressure across its surface. Assume the deflection x is small enough ($x \ll r$), then R can be expressed as $R \approx r^2/2x$. Then the biaxial stress σ can be given by[33]

$$\sigma = \Delta P r^2/4tx \tag{2}$$

In addition, the static deflection x at the center of the membrane is related to the pressure difference ΔP, and x can be expressed as[32]

$$\Delta P = \frac{4\sigma_0 t}{r^2}x + \frac{2Et}{(1-\nu)r^4}x^3 \tag{3}$$

where σ_0 is the pretension, ν is Poisson's ratio, and E is Young's modulus. The resonant frequency, f_{mn}, of a clamped circular membrane can be expressed as[33]

$$f_{mn} = \frac{\alpha_{mn}}{2\pi r}\sqrt{\frac{S}{\rho t}} \tag{4}$$

where α_{mn} is a constant and the subscripts m and n denote the numbers of the nodal diameter and nodal circle, respectively. Here, $\alpha_{01} = 2.404$, $\alpha_{11} = 3.832$, and $\alpha_{21} = 5.135$. S and ρ are the uniform tension per unit length of the boundary and the mass density, respectively; here, $S = \sigma t$. Combining eqs 2−4 and neglecting the prestress, the third power of the resonant frequency related to pressure difference ΔP can be expressed as[33]

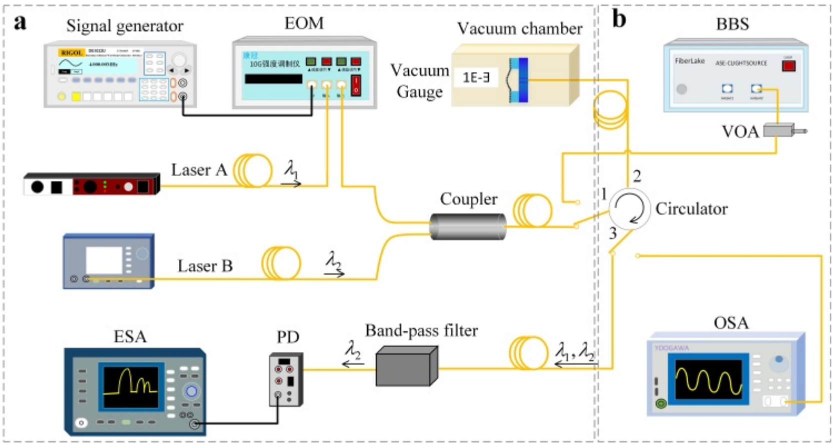

Figure 2. Experimental setup. (a) The all-fiber experimental apparatus used to monitor the response of the fiber tip resonator to changes in pressure. (b) The apparatus used to acquire optical reflection spectra. Legend: EOM, electro-optic modulator; PD, photodetector; ESA, electric spectrum analyzer; BBS, broad-band light source; VOA, variable optical attenuator; OSA, optical-spectrum analyzer.

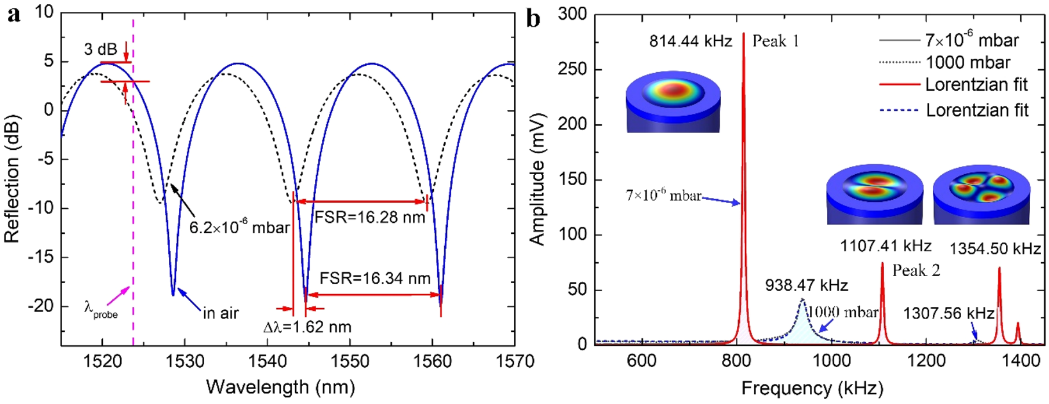

Figure 3. (a) Reflection spectra of a fiber tip resonator covered with a graphene membrane in air and in a vacuum chamber (6.2×10^{-6} mbar). (b) Amplitude as a function of frequency for the fiber tip resonator in air (1.0×10^3 mbar) and in a vacuum chamber (7×10^{-6} mbar).

$$f_{mn}^3 \approx \left(\frac{\alpha_{mn}}{2\pi r}\right)^3 \sqrt{\frac{2Er^2}{64(1-\nu)t^2\rho^3}}\,\Delta P \qquad (5)$$

From the above analysis, the resonant frequency f_{mn} of a circular membrane is affected by the pressure difference ΔP and the pretension σ_0.

The following should be noted. (a) The right side of eq 3 contains x twice, with exponents of 1 and 3, indicating that the membrane would be expected to respond to pressure changes in a nonlinear manner, such that shifts in the resonant frequency would also be nonlinear. If ΔP is large, the second term of eq 3 dominates, and the pressure response of the membrane is nonlinear under the large deformation. If ΔP is small enough, the first term of eq 3 dominates, and the pressure response of the membrane is linear, indicating the membrane is under the stress-dominated deformation. (b) The membrane is assumed to vibrate freely without being affected by any fluids. That is, the membrane is placed into a vacuum environment or the radius to thickness ratio of the membrane is relatively small;[33] otherwise, the effect of fluids should be considered. Moreover, eq 4 indicates that the higher-order resonant mode has higher sensitivity in the same pressure range, due to the larger constant α_{mn} of higher-order resonant modes.

The fabrication of the fiber tip pressure sensor involves three steps. In step 1, a section of HCF with an inner diameter of either 40 or 75 μm is spliced onto a commercial single-mode optical fiber (SMF, Corning Inc., SMF-28) using a fusion splicer (Fujikura, FSM-62S) in the manual operation mode. The end of the HCF is subsequently cleanly cleaved using a standard fiber cleaver under a microscope such that there is a distance, L, between the end and the splicing joint. This hollow cavity length is the initial Fabry−Pérot cavity length and is varied from 20 to 60 μm in this work. In step 2, a commercial MLG membrane (6 Carbon Technology, Shenzhen, China) grown on a copper foil having a thickness of 20 μm by chemical vapor deposition is transferred onto the HCF end facet using a wet transfer method. This transfer process has been described in detail in a prior publication.[34] MLG membranes with thicknesses ranging from 10 to 15 layers were used to ensure that the membrane was not permeable to air through any defects in the crystalline graphene, while still permitting easy manipulation and providing high optical reflectivity and good fabrication yields. In step 3, the surface of the MLG is sputter-coated with a thin layer of Au by magnetron sputtering to further improve the optical reflectivity of the material and so increase the signal-to-noise ratio during demodulation.[35] The Au thickness can be controlled by adjusting the sputtering time during the sputtering, and a sputtering time of 330 s (thickness ∼20 nm) was adopted in this work.

Figure 1c presents a side view of the sensor unit comprising an SMF and a section of HCF. Figure 1d,e shows top view optical microscopy images of the MLG-covered end facets with inner diameters of 75 and 40 μm, respectively, while Figure 1f,g provides the corresponding scanning electron microscopy images.

Figure 2a shows the all-optical-fiber system used for optical actuation and monitoring of the fiber tip resonator signal. A 1549.7000 nm amplitude-modulated low-noise single-frequency laser (laser A in this figure, Knheras ADJUSTIK E15 PM FM, Luster Light Tech International Co., Ltd.) with a tunable power output was employed to actuate the resonator. The laser intensity was modulated through an electro-optic modulator (EOM; Beijing Conquer Optics

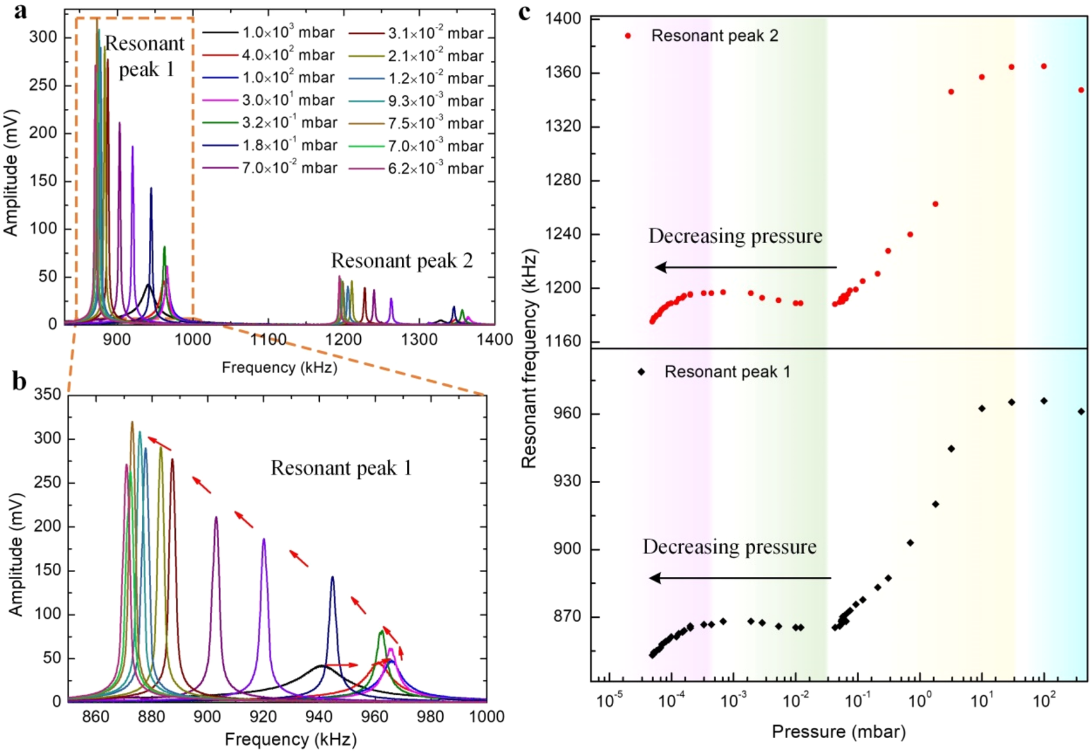

Figure 4. (a) Frequency spectra obtained from the ESA at different pressures. (b) Enlarged partial view of the region in the dotted box. (c) Resonant frequencies of the fundamental resonant mode and the second resonant mode of the clamped circular graphene membrane as functions of pressures.

Science & Technology Co., Ltd.) in conjunction with frequency modulation via a signal generator (DG1022U, Rigol Technologies, Inc.). This modulated optical heating of laser A was a time-variable local heating and would be absorbed by the graphene diaphragm, such that the graphene diaphragm thermally expands and contracts periodically. This expansion and contraction of the membrane is similar to the application of point-type thermoelastic excitation to a suspended graphene membrane, resulting in the resonance of the membrane. Simultaneously, another tunable laser (laser B, Agilent 81940A) with an output at 1524.6284 nm was employed to monitor the resulting membrane motion. The probe laser was detuned from the optical resonance to the point of maximum slope with respect to the cavity dispersion to optimize the transduction of vibrational signals. Herein, the wavelength of the probe laser is highlighted with a magenta dashed line in Figure 3a. The light beams emitted by both lasers A and B were coupled via a 2 × 1 coupler at a coupling ratio of 90:10 and then input into the fiber tip resonator through a three-port circulator. The resulting vibration of the Au/graphene membrane modulated the intensity of the laser B light beam reflected by the silica fiber end and the Au/graphene surface. After separating the reflected light with a wavelength of 1549.7000 nm by passing the beam through a tunable band-pass filter (TBF-1550−1.0-FCAPC, Newport), the light intensity was determined by a photodetector comprising a 10 MHz adjustable photoreceiver (Model 2053, New Fucus, Inc.) in conjunction with a preamplifier via the circulator. The light intensity signal was further processed using an electrical spectrum analyzer (ESA, R&S FSV4, Rohde & Schwarz).

Figure 2b provides a diagram of the instrumentation used to acquire optical reflection spectra. A broad-band light source, variable optical attenuator, circulator, and OSA with a resolution of 0.02 nm over the wavelength range of 600−1700 nm were employed to obtain the reflection spectra of the fiber tip resonators.

3. RESULTS AND DISCUSSION

Figure 3a shows the reflection spectra of the fiber tip resonator with an inner diameter of 40 μm covered with an Au/graphene membrane both in air and in a vacuum chamber (at a pressure of 6.2×10^{-6} mbar). The length of the Fabry−Pérot cavity, L_{FP}, can be calculated according to the equation[36]

$$L_{\text{FP}} = \frac{\lambda_m \lambda_{m-1}}{2 n_{\text{eff}} \text{FSR}_{(m,m-1)}} \tag{6}$$

where λ_m is the resonant wavelength of the mth order interference dip/peak, n_{eff} is the effective index of the intracavity medium, and $\text{FSR}_{(m,m-1)}$ is the free spectral range of the interference spectrum. On this basis, the calculated cavity lengths were 73.782 and 73.896 μm for the trials at ambient pressure and under a vacuum, respectively. Thus, the cavity length changed by approximately 114 nm on going from ambient pressure to a vacuum of 6.2×10^{-6} mbar. This value is much less than that obtained in a prior study,[32] possibly as a result of air leakage out of the sealed cavity in the present work.[9] Although graphene itself is impermeable to gases, leakage might occur along the van der Waals interface between the two-dimensional layers and the HCF end facet[9] as a result of nonideal adhesion of the graphene layer to the rough facet end.[13] It is also evident that the fringe contrast of the reflection spectrum decreased from approximately 25 to 13 dB as the pressure changed from atmospheric pressure to a vacuum. We attribute this to variations in the flatness of the graphene membrane as the pressure changed.[37] The reflectivity of the Au/graphene membrane is very sensitive to pressure because increased pressure will change the flatness of the membrane. The membrane will stretch as it deflects upward or downward as a result of a pressure difference, resulting in a change in the optical intensity reflected from the Au/graphene that might lead to variations in the fringe contrast.

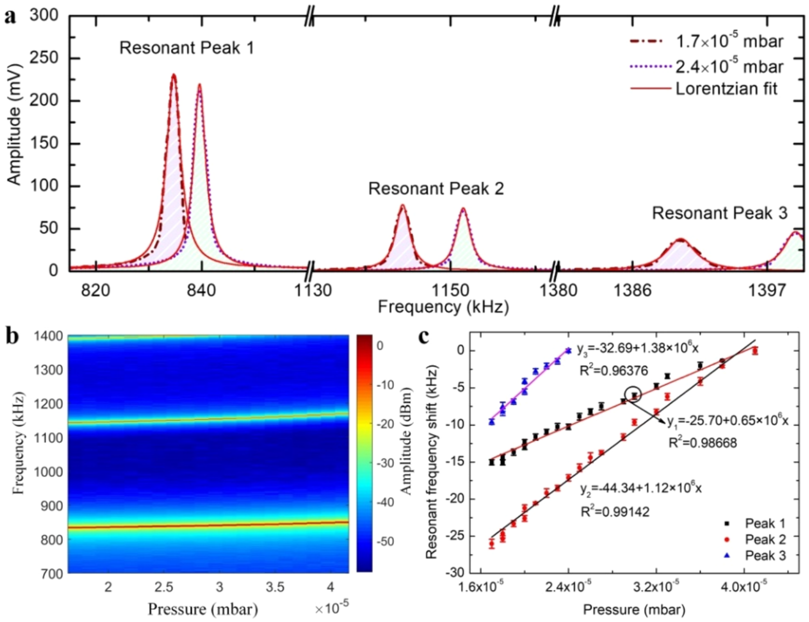

Figure 5. Pressure-dependent resonance. (a) The frequency spectra at 1.7×10^{-5} and 2.4×10^{-5} mbar. (b) Contour graph of the ESA frequency spectra at various pressures. (c) Resonant frequencies versus pressure within the range of 1.7×10^{-5} to 4.1×10^{-5} mbar. The error bar is obtained by a fast repeating sweep three times in each pressure measurement.

Figure 3b plots the amplitude as a function of frequency for a clamped circular graphene membrane at ambient pressure (1.0×10^3 mbar) and in a vacuum chamber (7×10^{-6} mbar). Four resonant peaks are evident at 814.44, 1107.41, 1354.5, and 1393.78 kHz in the plot of the vacuum data, and the peak with the lowest frequency of 814.44 kHz has the highest amplitude of 283.09 mV. In contrast, only two resonant peaks (at 938.47 and 1307.56 kHz) were obtained at atmospheric pressure. These two peaks exhibit relatively low amplitudes of 42.54 and 4.24 mV, which can possibly be attributed to the damping effect as the membrane vibrates in air. Both of these peaks exhibit a large shift after the pressure changes from 1000 to 7×10^{-6} mbar at room temperature, and a frequency shift of 124.03 kHz was observed in the case of resonant peak 1. The red solid and blue dashed curves show fittings of the experimental data. The inset figures provide images showing the three corresponding mechanical resonant modes as generated using the COMSOL Multiphysics software package.

The effect of pressure on the resonant frequency of the sensor was assessed by placing the device in a vacuum chamber and decreasing the pressure at a constant rate. During these trials, the pressure in the chamber was monitored using a digital compound vacuum gauge (XG5227-II, Jining Xinguang Vacuum Technology Co., Ltd.). Throughout this process, the ESA continually acquired frequency spectra between 700 and 1400 kHz at a rate of approximately one sweep every 26 s. Figure 4a presents a series of frequency spectra acquired at different pressures from 1.0×10^3 to 6.2×10^{-3} mbar. Two resonant modes are evident at all pressures. At higher pressures, the Q factors of both the fundamental and the second-order mode frequencies are seen to decrease. The peak resonant frequencies at the various pressures are seen more clearly in Figure 4b, which provides an enlarged view of the spectral region in the dotted box in Figure 4a. In these data a turning point is clearly observed near a pressure of 100 mbar. The resonant peak frequencies are plotted as functions of pressure in Figure 4c. Overall, the two frequency responses of the resonant modes show similar trends in response to pressure changes. In previous reports, the pressure range from atmospheric pressure to high vacuum has generally been divided into three different regions,[38] while four different regions are observed in this work. The resonant frequency of the membrane is seen to increase with decreases in the pressure from approximately 5×10^{-2} to 5×10^{-4} mbar and also at pressures above 100 mbar, which is similar to previous reports.[38] However, the resonant frequency decreases as the pressure decreases over the range of 100 to 5×10^{-2} mbar and below 5×10^{-4} mbar. There are three main energy dissipation mechanisms[38] for this mechanical resonator. First, losses to the surrounding fluid medium may occur as a result of acoustic radiation or viscous drag. Second, clamping or support losses may occur because of energy transfer to the support on which the device is mounted. Last, bulk losses based on physical mechanisms such as thermoelastic dissipation, internal friction, the motion of lattice defects, phonon−phonon scattering, and piezoelectric damping are possible. However, the contributions of these energy dissipation mechanisms to the total energy loss of the system are not equal and can vary with pressure changes. In the vicinity of atmospheric pressure, the ambient air acts as a viscous fluid and so medium damping is dominant. Conversely, under a high vacuum, bulk losses are the dominant dissipation mechanism. Between these two extremes, in the molecular flow region, surface dissipation is the dominant loss as a consequence of collisions between air molecules and the moving surface of the resonator. In addition, the airflow during the pressure decrease process in the chamber may affect the resonant frequency of the resonator because of gas leakage from the sealed cavity. In the ultrahigh-vacuum region (pressures lower than 5×10^{-4} mbar) the squeeze damping effect[39,40] might also play a role. Furthermore, the thermal conductivity of the ambient air decreases as the pressure decreases, such that the temperature of the graphene membrane increases. Because the thermal expansion coefficient of graphene is negative,[41,42] higher temperatures would be

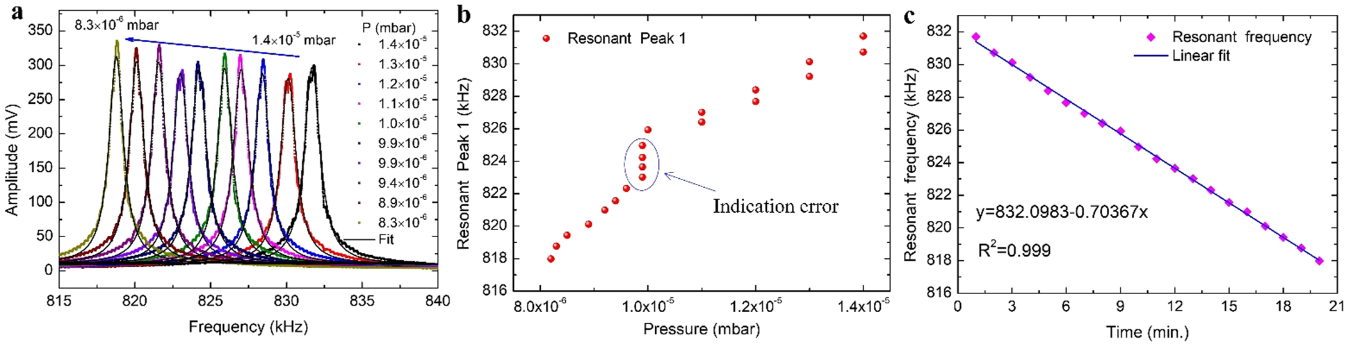

Figure 6. Fundamental resonant mode frequencies as a function of the air pressure. (a) Evolution of the frequency spectra of the sensor as the pressure is decreased from 1.4 × 10$^{−5}$ to 8.3 × 10$^{−6}$ mbar. (b) Resonant frequency peak value versus pressure. (c) Resonant frequency peak value versus time.

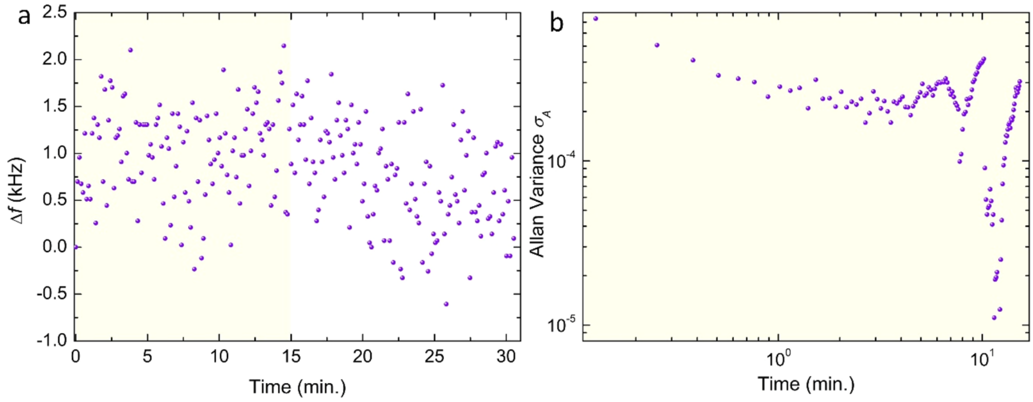

Figure 7. Experimental assessments of frequency stability. (a) Resonance frequency vs time for the Au/graphene membrane-based pressure sensor. (b) Extracted Allan variance data as a function of time.

expected to increase the stress experienced by the membrane and so to increase the resonant frequency of the graphene membrane. In addition, the Au coating, which has a positive thermal expansion coefficient, may also have an effect by decreasing the resonant frequency. Similar pressure−resonance frequency relationships have been reported.[43,44] Note that pure MLG deposited on the HCF end is not suitable for pressure sensing within a large pressure range because, in the large pressure range, the large Δ*P* will lead to a large deflection *x*, resulting in a small optical reflectivity of the material and so decrease the signal-to-noise ratio during demodulation.

The frequency spectra acquired at 1.7 × 10$^{−5}$ and 2.4 × 10$^{−5}$ mbar are plotted using wine and violet dotted lines, respectively, in Figure 5a, in which the red lines are the Lorentzian fitting results for the experimental data. Resonant peak 3 is seen to be partially missing at 2.4 × 10$^{−5}$ mbar because it is higher than 1400 kHz and so outside of the measured range of 700−1400 kHz. Figure 5b presents the frequency spectra acquired during a pressure ramp over the range of 1.7 × 10$^{−5}$ to 4.1 × 10$^{−5}$ mbar as a contour plot. The frequencies of the first, second, and third resonant modes are seen to increase along with the pressure. For all modes, the intensity shows slight fluctuations with changes in pressure and this effect can possibly be ascribed to imprecisions arising from the fitting process. The resonant frequency data are plotted versus pressure in Figure 5c. Here, the frequencies of the first, second, and third resonant modes all exhibit a linear shift to lower values as the pressure decreases. From these data, the pressure sensitivity values of the sensor were calculated to be 0.65 × 10^6, 1.12 × 10^6, and 1.38 × 10^6 kHz/mbar for the first, second, and third resonant modes based on linear fits within the pressure range of 1.7 × 10$^{−5}$ to 4.1 × 10$^{−5}$ mbar. The higher-order resonant modes provided higher sensitivity within the same pressure range, indicating that the sensitivity of this device could potentially be improved by monitoring higher-order modes.

To further assess the minimum detectable pressure difference that could be observed using the resonator at ultrahigh vacuum pressure, we acquired the first resonant mode frequency spectra from 700 to 960 kHz at a rate of approximately one sweep every 71 s. In these trials, the intermediate frequency bandwidth of the ESA was set at 500 Hz. Figure 6a shows the resulting spectra that were obtained as the pressure was gradually decreased from 1.4 × 10$^{−5}$ to 8.3 × 10$^{−6}$ mbar. A shift in the resonant frequency to lower values is clearly observed, as indicated by the blue arrow. This shift was also approximately linear as the applied pressure was decreased and the minimum detectable pressure difference was determined to be smaller than 1 × 10$^{−7}$ mbar (Figure 6b). This value is competitive with the detection limit of a commercially available digital vacuum gauge. Moreover, the digital commercial vacuum gauge displayed only two significant figures, resulting in indication errors shown in Figure 6b. To remove any effects resulting from the imprecisions of the commercial vacuum gauge readings, the resonant frequency peak was also plotted as a function of time, as shown in Figure 6c. The data clearly form a straight line at these ultrahigh-vacuum pressures, presumably because the pressure decreased at a constant rate within this narrow pressure range. From these data, the pressure sensitivity of the sensor was calculated to be −0.70 kHz/min by applying a linear fit to the resonant frequency peak values.

The concept detection limit (DL) of the sensor was first introduced by White et al.[45] as

$$\mathrm{DL} = \frac{R_s}{S_s} \tag{7}$$

where S_s and R_s are the sensitivity and resolution of the sensor, respectively. The resolution of the sensor R_s can be approximately calculated by individual noise variances, that is $R_s = 3\delta$.

$$\delta \approx \frac{\Delta f_F}{4.5(\mathrm{SNR}^{0.25})} \tag{8}$$

Here, Δf_F is the full-width at half-maximum (FWHM) of the resonant mode frequency. SNR is the signal-to-noise ratio. In our pressure-sensing experiment, the main restriction of the detection limit is the FWHM. The measured value of FWHM is ∼1.2 kHz, and the SNR expressed in a linear plot is ∼60 dB. The DL of the device is calculated to be $\sim 3.9 \times 10^{-8}$ mbar. Thus, the detectable pressure difference of 1×10^{-7} mbar taken from Figure 6b is reasonable. Moreover, we investigated the frequency stability of the resonator by performing measurements over time at a constant pressure. The frequency data were plotted over time, as shown in Figure 7a. The frequency measurement error could be characterized using the Allan deviation, defined as[11]

$$\sigma_A = \frac{1}{f_0}\sqrt{\frac{1}{2(N-1)}\sum_{j=2}^{N}(f_j - f_{j-1})^2} \tag{9}$$

where f_j is the resonance frequency extracted at the jth measurement in Figure 7a. As shown in Figure 7b, a minimum value of Allan variance $\sigma_A = 5.717 \times 10^{-6}$ was obtained at $\tau = 11.9568$ min, corresponding to a minimum detectable frequency shift δf of $\sigma_A \times f_0 = 4.65 \times 10^{-3}$ kHz. Thus, a pressure resolution δP of 7.16×10^{-9} mbar was obtained by using the equation $\delta P = \text{sensitivity} \times \delta f$, where the sensitivity is the first-order mode in mbar/kHz and δf is the intrinsic inaccuracy in the resonance frequency determination.

4. CONCLUSION

This work demonstrated an all-fiber optomechanical pressure sensor based on a clamped circular graphene membrane. A uniform pressure load was employed to deform the membrane, resulting in a change in its resonant frequency. Using this method, we obtained a pressure sensor with a resolution as small as 7.16×10^{-9} mbar. Moreover, this pressure sensor can work over an extended pressure range of 7×10^{-6} to 1000 mbar at room temperature. Such an extended range of pressure indicate that the present device outperforms commercial sensors. Furthermore, monitoring higher-order resonant frequencies gave the same general trends as were observed for the fundamental resonant frequency but provided better pressure sensitivity within the same pressure range. Therefore, the pressure sensitivity could potentially be improved by monitoring higher-order modes. The micrometer size scale, absence of on-chip power requirements, high resolution, and fast response of the proposed optomechanical pressure sensor indicate great potential for real-world long-distance pressure detection applications.

■ ASSOCIATED CONTENT

Data Availability Statement

Data underlying the results presented in this paper are not publicly available at this time but may be obtained from the authors upon reasonable request.

■ AUTHOR INFORMATION

Corresponding Author

Shen Liu − *Shenzhen Key Laboratory of Photonic Devices and Sensing Systems for Internet of Things, Guangdong and Hong Kong Joint Research Centre for Optical Fiber Sensors, and Key Laboratory of Optoelectronic Devices and Systems of the Ministry of Education and Guangdong Province, College of Physics and Optoelectronic Engineering, Shenzhen University, Shenzhen 518060, People's Republic of China;* orcid.org/0000-0001-9266-2498; Email: shenliu@szu.edu.cn

Authors

Yanping Chen − *Shenzhen Key Laboratory of Photonic Devices and Sensing Systems for Internet of Things, Guangdong and Hong Kong Joint Research Centre for Optical Fiber Sensors, and Key Laboratory of Optoelectronic Devices and Systems of the Ministry of Education and Guangdong Province, College of Physics and Optoelectronic Engineering, Shenzhen University, Shenzhen 518060, People's Republic of China*

Guiqing Hong − *Shenzhen Key Laboratory of Photonic Devices and Sensing Systems for Internet of Things, Guangdong and Hong Kong Joint Research Centre for Optical Fiber Sensors, and Key Laboratory of Optoelectronic Devices and Systems of the Ministry of Education and Guangdong Province, College of Physics and Optoelectronic Engineering, Shenzhen University, Shenzhen 518060, People's Republic of China*

Mengqiang Zou − *Shenzhen Key Laboratory of Photonic Devices and Sensing Systems for Internet of Things, Guangdong and Hong Kong Joint Research Centre for Optical Fiber Sensors, and Key Laboratory of Optoelectronic Devices and Systems of the Ministry of Education and Guangdong Province, College of Physics and Optoelectronic Engineering, Shenzhen University, Shenzhen 518060, People's Republic of China*

Bonan Liu − *Shenzhen Key Laboratory of Photonic Devices and Sensing Systems for Internet of Things, Guangdong and Hong Kong Joint Research Centre for Optical Fiber Sensors, and Key Laboratory of Optoelectronic Devices and Systems of the Ministry of Education and Guangdong Province, College of Physics and Optoelectronic Engineering, Shenzhen University, Shenzhen 518060, People's Republic of China*

Junxian Luo − *Shenzhen Key Laboratory of Photonic Devices and Sensing Systems for Internet of Things, Guangdong and Hong Kong Joint Research Centre for Optical Fiber Sensors, and Key Laboratory of Optoelectronic Devices and Systems of the Ministry of Education and Guangdong Province, College of Physics and Optoelectronic Engineering, Shenzhen University, Shenzhen 518060, People's Republic of China*

Yiping Wang − *Shenzhen Key Laboratory of Photonic Devices and Sensing Systems for Internet of Things, Guangdong and Hong Kong Joint Research Centre for Optical Fiber Sensors, and Key Laboratory of Optoelectronic Devices and Systems of* *the Ministry of Education and Guangdong Province, College of Physics and Optoelectronic Engineering, Shenzhen University, Shenzhen 518060, People's Republic of China*

Complete contact information is available at:
https://pubs.acs.org/10.1021/acsami.2c09865

Author Contributions

Y.C. and S.L. jointly conceived the idea. Y.C. designed and fabricated the devices, built the experimental setup, and carried out the experiments. Y.C., S.L., G.H., J.L., and B.L. analyzed the data. S.L. and Y.W. assisted with the theory. M.Z. developed the modeling. Y.C. wrote the manuscript, and S.L. edited the manuscript with contributions from all coauthors. All authors have given approval to the final version of the manuscript.

Notes

The authors declare no competing financial interest.

■ ACKNOWLEDGMENTS

This study was supported by the National Natural Science Foundation of China (NSFC) (grant nos. 62175165 and 61905165), the Guangdong Basic and Applied Basic Research Foundation (grant no. 2021A1515011834), the Shenzhen Science and Technology Program (grant nos. RCBS20200714114922296 and JCYJ20210324120403009), and the Postgraduate Innovation Development Fund Project of Shenzhen University (grant no. 315-0000470804). We thank Liwen Bianji (Edanz) (https://www.liwenbianji.cn) for editing the language of a draft of this manuscript.

■ REFERENCES

(1) Ricci, F.; Cuairan, M. T.; Conangla, G. P.; Schell, A. W.; Quidant, R. Accurate Mass Measurement of a Levitated Nanomechanical Resonator for Precision Force-Sensing. *Nano Lett.* **2019**, *19* (10), 6711−6715.

(2) Lassagne, B.; Tarakanov, Y.; Kinaret, J.; Garcia-Sanchez, D.; Bachtold, A. Coupling mechanics to charge transport in carbon nanotube mechanical resonators. *Science* **2009**, *325* (5944), 1107−10.

(3) Zheng, B.-C.; Yan, S.-C.; Chen, J.-H.; Cui, G.-X.; Xu, F.; Lu, Y.-Q. Miniature optical fiber current sensor based on a graphene membrane. *Laser Photonics Rev.* **2015**, *9* (5), 517−522.

(4) Malvar, O.; Ruz, J. J.; Kosaka, P. M.; Dominguez, C. M.; Gil-Santos, E.; Calleja, M.; Tamayo, J. Mass and stiffness spectrometry of nanoparticles and whole intact bacteria by multimode nanomechanical resonators. *Nat. Commun.* **2016**, *7*, 13452.

(5) Gruber, G.; Urgell, C.; Tavernarakis, A.; Stavrinadis, A.; Tepsic, S.; Magen, C.; Sangiao, S.; de Teresa, J. M.; Verlot, P.; Bachtold, A. Mass Sensing for the Advanced Fabrication of Nanomechanical Resonators. *Nano Lett.* **2019**, *19* (10), 6987−6992.

(6) Jensen, K.; Kim, K.; Zettl, A. An atomic-resolution nanomechanical mass sensor. *Nat. Nanotechnol.* **2008**, *3* (9), 533−7.

(7) Sage, E.; Brenac, A.; Alava, T.; Morel, R.; Dupre, C.; Hanay, M. S.; Roukes, M. L.; Duraffourg, L.; Masselon, C.; Hentz, S. Neutral particle mass spectrometry with nanomechanical systems. *Nat. Commun.* **2015**, *6*, 6482.

(8) Chen, Y. M.; He, S. M.; Huang, C. H.; Huang, C. C.; Shih, W. P.; Chu, C. L.; Kong, J.; Li, J.; Su, C. Y. Ultra-large suspended graphene as a highly elastic membrane for capacitive pressure sensors. *Nanoscale* **2016**, *8* (6), 3555−64.

(9) Lee, M.; Davidovikj, D.; Sajadi, B.; Siskins, M.; Alijani, F.; van der Zant, H. S. J.; Steeneken, P. G. Sealing Graphene Nanodrums. *Nano Lett.* **2019**, *19* (8), 5313−5318.

(10) Siskins, M.; Lee, M.; Manas-Valero, S.; Coronado, E.; Blanter, Y. M.; van der Zant, H. S. J.; Steeneken, P. G. Magnetic and electronic phase transitions probed by nanomechanical resonators. *Nat. Commun.* **2020**, *11* (1), 2698.

(11) Blaikie, A.; Miller, D.; Aleman, B. J. A fast and sensitive room-temperature graphene nanomechanical bolometer. *Nat. Commun.* **2019**, *10* (1), 4726.

(12) Bunch, J. S.; Zande, A.; Verbridge, S. S.; Frank, I. W.; Tanenbaum, D. M.; Parpia, J. M.; Craighead, H. G.; Mceuen, P. L. Electromechanical Resonators from Graphene Sheets. *Science* **2007**, *315* (5811), 490−493.

(13) Bunch, J. S.; Verbridge, S. S.; Alden, J. S.; Van, D.; Parpia, J. M.; Craighead, H. G.; Mceuen, P. L. Impermeable Atomic Membranes from Graphene Sheets. *Nano Lett.* **2008**, *8* (8), 2458−2462.

(14) Sun, P. Z.; Yang, Q.; Kuang, W. J.; Stebunov, Y. V.; Xiong, W. Q.; Yu, J.; Nair, R. R.; Katsnelson, M. I.; Yuan, S. J.; Grigorieva, I. V.; Lozada-Hidalgo, M.; Wang, F. C.; Geim, A. K. Limits on gas impermeability of graphene. *Nature* **2020**, *579* (7798), 229−232.

(15) Chen, J. H.; Jang, C.; Xiao, S.; Ishigami, M.; Fuhrer, M. S. Intrinsic and extrinsic performance limits of graphene devices on SiO2. *Nat. Nanotechnol.* **2008**, *3* (4), 206−9.

(16) Patel, R. N.; Mathew, J. P.; Borah, A.; Deshmukh, M. M. Low tension graphene drums for electromechanical pressure sensing. *2D Mater.* **2016**, *3* (1), 011003.

(17) Chen, C.; Rosenblatt, S.; Bolotin, K. I.; Kalb, W.; Kim, P.; Kymissis, I.; Stormer, H. L.; Heinz, T. F.; Hone, J. Performance of monolayer graphene nanomechanical resonators with electrical readout. *Nat. Nanotechnol.* **2009**, *4* (12), 861−7.

(18) Smith, A. D.; Niklaus, F.; Paussa, A.; Vaziri, S.; Fischer, A. C.; Sterner, M.; Forsberg, F.; Delin, A.; Esseni, D.; Palestri, P.; Ostling, M.; Lemme, M. C. Electromechanical piezoresistive sensing in suspended graphene membranes. *Nano Lett.* **2013**, *13* (7), 3237−42.

(19) Smith, A. D.; Vaziri, S.; Niklaus, F.; Fischer, A. C.; Sterner, M.; De Lin, A.; Östling, M.; Lemme, M. C. Pressure sensors based on suspended graphene membranes. *Solid-State Electron.* **2013**, *88*, 89−94.

(20) Smith, A. D.; Niklaus, F.; Paussa, A.; Schröder, S.; Fischer, A. C.; Sterner, M.; Wagner, S.; Vaziri, S.; Forsberg, F.; Esseni, D. Piezoresistive Properties of Suspended Graphene Membranes under Uniaxial and Biaxial Strain in Nanoelectromechanical Pressure Sensors. *ACS Nano* **2016**, *10*, 9879.

(21) Davidovikj, D.; Scheepers, P. H.; van der Zant, H. S. J.; Steeneken, P. G. Static Capacitive Pressure Sensing Using a Single Graphene Drum. *ACS Appl. Mater. Interfaces* **2017**, *9* (49), 43205−43210.

(22) Ikins, M.; Lee, M.; Wehenkel, D.; Rijn, R. V.; Steeneken, P. G. Sensitive capacitive pressure sensors based on graphene membrane arrays. *Microsyst. Nanoeng.* **2020**, *6* (102), 1−9.

(23) Liu, S.; Wang, Y.; Liao, C.; Wang, Y.; He, J.; Fu, C.; Yang, K.; Bai, Z.; Zhang, F. Nano silica diaphragm in-fiber cavity for gas pressure measurement. *Sci. Rep.* **2017**, *7* (1), 1−9.

(24) Wang, X.; Jiang, J.; Wang, S.; Liu, K.; Liu, T. All-silicon dual-cavity fiber-optic pressure sensor with ultralow pressure-temperature cross-sensitivity and wide working temperature range. *Photonics Res.* **2021**, *9* (4), 521.

(25) Guo, X.; Zhou, J.; Du, C.; Wang, X. Highly Sensitive Miniature All-Silica Fiber Tip Fabry-Perot Pressure Sensor. *IEEE Photonics Technol. Lett.* **2019**, *31* (9), 689−692.

(26) Chu, C.; Wang, J.; Qiu, J. Miniature High-Frequency Response, High-Pressure-Range Dynamic Pressure Sensor Based on All-Silica Optical Fiber Fabry-Perot Cavity. *IEEE Sens. J.* **2021**, *21* (12), 13296−13304.

(27) Wu, J.; Yao, M.; Xiong, F.; Zhang, A. P.; Tam, H.-Y.; Wai, P. K. A. Optical Fiber-Tip Fabry-Pérot Interferometric Pressure Sensor Based on anIn Situμ-Printed Air Cavity. *J. Lightwave Technol.* **2018**, *36* (17), 3618−3623.

(28) Chen, D.; Hu, G.; Chen, L. Dual-Core Photonic Crystal Fiber for Hydrostatic Pressure Sensing. *IEEE Photonics Technol. Lett.* **2011**, *23* (24), 1851−1853.

(29) Pereira, L. M.; Pospori, A.; Antunes, P.; Domingues, M. F.; Marques, S.; Bang, O.; Webb, D. J.; Marques, C. Phase-shifted Bragg

grating inscription in PMMA microstructured POF using 248 nm UV radiation. *J. Lightwave Technol.* **2017**, *35* (23), 5176−5184.
(30) Luo, J.; Liu, S.; Zhao, Y. Y.; Chen, Y.; Wang, Y.; et al. A phase-shifted FBG modulated by a hollow cavity for measuring gas pressure. *Opt. Lett.* **2020**, *45* (2), 507−510.
(31) Dong, N.; Wang, S.; Jiang, L.; Jiang, Y.; Wang, P.; Zhang, L. Pressure and Temperature Sensor Based on Graphene Diaphragm and Fiber Bragg Gratings. *IEEE Photonics Technol. Lett.* **2018**, *30* (5), 431−434.
(32) Ma, J.; Wei, J.; Ho, H. L.; Ji, Y. D. High-sensitivity fiber-tip pressure sensor with graphene diaphragm. *Opt. Lett.* **2012**, *37* (13), 2493−2495.
(33) Ma, J. Miniature fiber-tip Fabry-Perot interferometric sensors for pressure and acoustic detection; 2014.
(34) Ma, J.; Zhou, Y.; Bai, X.; Chen, K.; Guan, B. O. High-sensitivity and fast-response fiber-tip Fabry-Perot hydrogen sensor with suspended palladium-decorated graphene. *Nanoscale* **2019**, *11* (34), 15821−15827.
(35) Luo, J.; Liu, S.; Chen, P.; Lu, S.; Zhang, Q.; Chen, Y.; Du, B.; Tang, J.; He, J.; Liao, C.; Wang, Y. Fiber optic hydrogen sensor based on a Fabry-Perot interferometer with a fiber Bragg grating and a nanofilm. *Lab Chip* **2021**, *21*, 1752−1758.
(36) Liu, S.; Wang, Y.; Liao, C.; Wang, G.; Li, Z.; Wang, Q.; Zhou, J.; Yang, K.; Zhong, X.; Zhao, J.; Tang, J. High-sensitivity strain sensor based on in-fiber improved Fabry-Perot interferometer. *Opt. Lett.* **2014**, *39* (7), 2121−4.
(37) Liao, C.; Liu, S.; Xu, L.; Wang, C.; Wang, Y.; Li, Z.; Wang, Q.; Wang, D. N. Sub-micron silica diaphragm-based fiber-tip Fabry-Perot interferometer for pressure measurement. *Opt. Lett.* **2014**, *39* (10), 2827−30.
(38) Olfatnia, M.; Shen, Z.; Miao, J. M.; Ong, L. S.; Xu, T.; Ebrahimi, M. Medium damping influences on the resonant frequency and quality factor of piezoelectric circular microdiaphragm sensors. *J. Micromech. Microeng.* **2011**, *21* (4), 045002.
(39) Dolleman, R. J.; Chakraborty, D.; Ladiges, D. R.; van der Zant, H. S. J.; Sader, J. E.; Steeneken, P. G. Squeeze-Film Effect on Atomically Thin Resonators in the High-Pressure Limit. *Nano Lett.* **2021**, *21* (18), 7617−7624.
(40) Dolleman, R. J.; Davidovikj, D.; Cartamil-Bueno, S. J.; Zant, H. S. J. V. D.; Steeneken, P. G. Graphene Squeeze-Film Pressure Sensors. *Nano Lett.* **2015**, *16*, 568−571.
(41) Yoon, D.; Son, Y. W.; Cheong, H. Negative thermal expansion coefficient of graphene measured by Raman spectroscopy. *Nano Lett.* **2011**, *11* (8), 3227−31.
(42) Singh, V.; Sengupta, S.; Solanki, H. S.; Dhall, R.; Allain, A.; Dhara, S.; Pant, P.; Deshmukh, M. M. Probing thermal expansion of graphene and modal dispersion at low-temperature using graphene nanoelectromechanical systems resonators. *Nat. Nanotechnol.* **2010**, *21* (16), 165204.
(43) Inaba, S.; Hane, K. Resonance frequency shifts of a photothermal vibration in vacuum. *J. Vac. Sci. Technol. A* **1991**, *9* (4), 2138−2139.
(44) Hane, K.; Iwatuki, T.; Inaba, S.; Okuma, S. Frequency shift on a micromachined resonator excited photothermally in vacuum. *Rev. Sci. Instrum.* **1992**, *63* (7), 3781−3782.
(45) White, I. M.; Fan, X. On the performance quantification of resonant refractive index sensors. *Opt. Express* **2008**, *16* (2), 1020−1028.

https://doi.org/10.1021/acsami.2c09865
ACS Appl. Mater. Interfaces 2022, 14, 39211−39219